Advanced Computational Modeling for Growing III-V Materials in a High-Pressure Chemical Vapor-Deposition Reactor

Beatriz H. Cardelino*[a], Craig E. Moore[b], Carlos A. Cardelino[c], Nikolaus Dietz[d]

[a] Chemistry Department, Spelman College, Atlanta, GA 30314; corresponding author

[b] Space Sciences Laboratory, NASA Marshall Space Flight Center, Huntsville, AL 35812

[c] School of Earth and Atmospheric Sciences, Georgia Institute of Technology, Atlanta, GA 30332

[d] Department of Physics and Astronomy, Georgia State University, Atlanta, GA 30302

ABSTRACT

A numerical model was developed to simulate vapor deposition in high-pressure chemical vapor-deposition reactors, under different conditions of pressure, temperature, and flow rates. The model solved for steady-state gas-phase and heterogeneous chemical kinetic equations coupled with fluid dynamic equations within a three-dimensional grid simulating the actual reactor. The study was applied to indium nitride (InN) epitaxial growth. The steady-state model showed that at 1050-1290 K average substrate temperatures and 10 atm of total pressure, atomic indium (In) and monomethylindium [$In(CH_3)$] were the main group III gaseous species, and undissociated ammonia (NH_3) and amidogen (NH_2) the main group V gaseous species. The results from numerical models with an inlet mixture of 0.73:0.04:0.23 mass fraction ratios for nitrogen gas (N_2), NH_3 and trimethylindium [$In(CH_3)_3$], respectively, and an initial flow rate of 0.17 m s^{-1}, were compared with experimental values. Using a simple four-path surface reaction scheme, the numerical models yielded a growth rate of InN film of 0.027 μm per hour when the average substrate temperature was 1050 K and 0.094 μm per hour when the average substrate temperature was 1290 K. The experimental growth rate under similar flow ratios and reactor pressure, with a reactor temperature between 800 and 1150 K yielded an average growth rate of 0.081 μm per hour, comparing very well with the computed values.

III-V, modeling, OMCVD, HPCVD, indium nitride, photovoltaic, semiconductor, Terahertz, optoelectronics

1. INTRODUCTION

During the last ten years there has been much interest in the development of photovoltaic devices as energy sources for satellites and other space applications. Some of the advantages of using group III-V materials for these applications are: their high output power per square unit, their high radiation reliability, their large lifetimes in orbit, and their small efficiency change with temperature compared to silicon[1]. A way of improving solar cells for space applications is by expanding their spectral photosensitivity range, since solar radiation spans from 0.4 to 4 eV. But no single material can perfectly match that broad range. So tandem or cascade devices containing semiconductors with different band gaps can trap photons of different wavelengths and may be used to increase the efficiency of solar cells[2]. Recent improvements in the group III-nitride materials showed that tandem cells based on, for example, AlN-GaN-InN, have the potential for producing high-efficient solar cells[3]. Also, group III-nitrides are relatively insensitive to structural imperfections, making them suitable for environmentally harsh conditions[4]. Moreover, large second-harmonic enhancement has been observed in photonic crystals using group III-nitrides[5]. The wide band gap of group III-nitride semiconductors, coupled with large nonlinearities, is appealing for light control and manipulation in photonic structures.

The growth of group III-V semiconductor devices is most efficient by organometallic chemical vapor deposition (OMCVD). But InN epitaxial growth has a large thermal decomposition pressure at its optimum growth temperature. Epitaxy at lower than optimum temperatures and subatmospheric pressures is problematic because of its not well-

*cardelino@spelman.edu; phone 404-270-5741; fax 404-270-5752.

understood point defect chemistry that results in conflicting materials properties. Surface stabilization data showed that InN can be grown at much higher temperatures in high nitrogen pressures. Presently, good results have been achieved using high-pressure chemical vapor-deposition (HPCVD) reactors[6]. The development of high quality InN materials and related alloys open a wide field of novel devices, applicable to high-efficient energy conversion (solar cells and solid-state lighting) and high speed optoelectronics for optical communication systems, as well as for semiconductor laser operating into the blue and ultraviolet regions. It also holds a potential for spintronic device structures[7] and as a Terahertz emitter[8].

In order to gain a more detailed understanding of the growth process of InN and to foster the search of novel approaches to produce new materials, we have developed a computational model for simulating vapor deposition in reactors under different conditions of pressure, temperature, flow rates, and gravity. This numerical model couples complex chemical kinetics with fluid dynamic properties within a three-dimensional grid that simulates the reactor. The source compounds are trimethylindium [$In(CH_3)_3$] and ammonia (NH_3), which are the basis for the chemistry.

2. METHOD

Due to the complexity of the chemistry, we followed two different computational approaches:

(1) a time-evolution model, based on chemical kinetic equations, and
(2) a steady-state model with the chemical species flowing in a high-pressure vapor-phase deposition reactor, governed by fluid dynamic and chemical kinetic equations.

The evolution modeling was performed using MATLAB[9], and the steady-state modeling used CFD-ACE[10].

The evolution model represented the reactor as a single volume that was kept at a constant temperature and pressure. Simulations with the evolution model were used mainly to generate realistic reduced sets of chemical equations for the steady-state model. The steady-state model represented the reactor with a three-dimensional grid of 97,000 hexagonal cells at different temperatures, with varied flow velocities and constant pressure. After a finite number of iterations, the steady-state simulations provided a snapshot of the distributions of mass fractions of the different species at the different grid volumes.

The evolution model at constant temperature and pressure required values of reaction rate constants at a single temperature and pressure. The steady-state model required parameters for the computation of mass and heat transport, as well as reaction rate constants, at a wide range of temperatures but at a fixed pressure.

2.1 Gas-phase reactions

The gas-phase reactions considered are described in Table 1. They are grouped as follows:

(a) the dissociation reactions of the group III source gas [trimethylindium: $In(CH_3)_3$] (Reactions 1-4);
(b) the dissociation reactions of the group V source gas [ammonia: NH_3] (Reactions 5-7);
(c) the formation of methylated ammonia derivatives [trimethylamine, dimethylamine, methylamine: $N(CH_3)_3$, $NH(CH_2)_2$, $NH_2(CH_3)$] and their dissociation reactions (Reactions 8-16);
(d) all possible adduct formations between group III and group V species, and the subsequent release of a methyl group or a hydrogen atom (Reactions 17-75).
(e) the termination reactions which include the formation of ethane (C_2H_6), methane (CH_4), nitrogen gas (N_2), and hydrogen gas (H_2) (Reactions 76-79).

The above set of gas-phase reactions includes 47 species. The possible dissociation of carbon-hydrogen bonds was neglected and methyl groups were assumed to be undissociable units. Forward reactions in the gas phase were taken to be homolytic dissociations and the reaction rate constants were calculated using transition-state theory. The reverse reaction rate constant was calculated using the equilibrium constant for the forward reaction.

2.2 Deposition, etching and surface reactions

The species considered for deposition were (Table 1, reactions 80-83): (a) indium nitride (InN), (b) atomic indium (In), (c) monomethylindium ($InCH_3$), and (d) the indium amine radical ($InNH_2$). The surface reactions considered were (Table 1, reactions 84-88): (a) the capture of NH_2 by adsorbed In to form adsorbed $InNH_2$; (b) the dissociation of adsorbed $InNH_2$ into adsorbed InN and H_2; (c) the capture of NH by adsorbed $InCH_3$ to form adsorbed $In(CH_3)NH$; (d)

the dissociation of adsorbed $In(CH_3)NH$ into adsorbed InN and methane (CH_4); and (e) the decomposition of adsorbed InN into adsorbed In and atomic N. The symbol _S in reactions 80-88 represents the adsorbed species. The following equations summarize the heterogeneous chemistry model: depositions (left) and surface reactions (right).

[1] $InN \leftrightarrow InN\_S$
[2] $In \leftrightarrow In\_S$
[3] $InCH_3 \leftrightarrow InCH_3\_S$
[4] $InNH_2 \leftrightarrow InNH_2\_S$

[5] $In\_S + NH_2 \leftrightarrow InNH_2\_S$
[6] $InNH_2\_S \leftrightarrow InN\_S + H_2$
[7] $InCH_3\_S + NH \leftrightarrow In(CH_3)NH\_S$
[8] $In(CH_3)NH\_S \leftrightarrow InN\_S + CH_4$
[9] $InN\_S \rightarrow In\_S + N$

The deposition rate constants ([1] to [4]) were calculated using kinetic theory of gases. The desorption rate constants were calculated from the equilibrium constant and the deposition rate constant. The surface reactions [5], [7] and [9] were calculated from the reverse homolytic dissociations, and reactions [6] and [8] were assumed to be single-step elementary reactions.

2.3 Computational details of reaction rate constants in the gas phase

The values of the rate constants were obtained using a semiclassical approach based on transition state theory and quantum mechanical computations using the GAUSSIAN 2003 software package[11]. The quantum mechanical computations used density functional theory[12] and extensive basis sets, particularly on the indium atom.

The procedure for calculating the homolytic rate constants was based on the Rice-Ramsperger-Kassel-Marcus[13] theory. The Troe approach was used for calculating the bimolecular component of the unimolecular rate constants[14]. The procedure allowed for a real-gas correction using a compressibility factor obtained from a virial correction and derived from Lennard-Jones parameters (please see below). The calculation accounted for the presence of internal rotations in the species. All reactions were obtained in a nitrogen gas bath.

We have previously applied this method to groups III and V source vapor molecules for organometallic chemical vapor deposition[15]. Comparison of predicted reaction rate constants with experimentally determined values showed that the predicted reaction rates compared well to the uncertainty of the measurements. Please refer to that article for the pertinent equations.

2.4 Computational details of surface reaction rate constants

The deposition, etching and surface reaction rate constants will be calculated in the future from first principles, using the ONIOM approach[16]. In the meantime, we have used approximated rate constant values.

The rate constants for the deposition reactions were based on a calculation of the number of collisions (Z) against a 1-cm^2 substrate (A), and the partial pressure of the species.

[9] $$Z = \frac{P_{InN}}{k_B T}\sqrt{\frac{k_B T}{2\,\pi\, m}}\,A$$

The rate constants for the opposite reactions were calculated from the equilibrium constants for the adsorption reactions. These latter constants were estimated using reported values by Sengupta et al.[17] as follows: their reported forward and reverse rate constants for the adsorption of $GaCH_3$, $GaNH_2$ and NH_2 were used to calculate equilibrium constants for the adsorption reactions of those species; from those values, an average Gibbs free energy of formation for adsorption was estimated; using that average Gibbs free energy of formation and our temperature-dependent coefficients for the species corresponding to our adsorption reactions, we estimated the equilibrium constants for our reactions.

As was previously mentioned, the dissociation of the adsorbed species $InNH_2$ and $InCH_3NH$ into H_2 or CH_4, respectively, was assumed to be a single step dissociation. Reaction rate constants were computed for 18 pressures from 1 to 100 atm and for a range of temperatures between 300 and 1400 K. For the variable-temperature models it was necessary to fit the data into the following equation:

[10] $$k = A\,T^n\,e^{\frac{-Ea}{RT}}$$

2.5 Parameters for the transport properties

We calculated Lennard-Jones and Sutherland parameters for all 47 species. The Lennard-Jones parameters (ε_{LJ} and σ_{LB}) were obtained by using equations derived from fitting ninety empirical values to the number of electrons (n) in the molecule. The equations used were:

$$[11] \quad \frac{\varepsilon_{LJ}}{k_B} = 15.263\, n^{0.7726} \qquad R^2 = 0.75 \qquad [12] \quad \sigma_{LJ} = 2.3132\, n^{0.1871} \qquad R^2 = 0.61$$

where k_B is Boltzmann constant. The Sutherland parameters (A, B, and C) were obtained using the values of the Lennard-Jones potential for intermolecular distances beyond the inflexion point of the potential, and using an empirical fit of the C value as a function of j from viscosity and diffusion data. The equations used were:

$$[13] \quad U_{Su} \approx U_{LJ \text{ for large } r} = -\frac{\varepsilon_{Su}}{k_B}\left(\frac{\sigma_{Su}}{r}\right)^j \qquad [15] \quad B = C\frac{\varepsilon_{Su}}{k_B}$$

$$[14] \quad A = \sqrt{\frac{R}{M}}\frac{1}{\pi^{3/2}\sigma_{Su}^2} \qquad [16] \quad C = -7.19\text{x}10^{-2} \ln j + 0.299 \qquad R^2 = 0.9997$$

where R is the ideal gas constant and M the molar mass. The CFD-ACE program computes viscosity, diffusion and thermal conductivity based on these parameters.

2.6 Thermodynamic parameters

The heat capacity (C_p), enthalpy (H) and entropy (S) were expressed in terms of the following polynomial expressions on T, used by the JANAF tables[18]:

$$[17] \quad \frac{C_p}{R} = z_1 + z_2 T + z_3 T^2 + z_4 T^3 + z_5 T^4$$

$$[18] \quad \frac{H}{R} = z_1 T + \frac{z_2}{2} T^2 + \frac{z_3}{3} T^3 + \frac{z_4}{4} T^4 + \frac{z_5}{5} T^5 + z_6$$

$$[19] \quad \frac{S}{R} = z_1 \ln T + z_2 T + \frac{z_3}{2} T^2 + \frac{z_4}{3} T^3 + \frac{z_5}{4} T^4 + z_7$$

where z_6 corresponds to the heat-of-formation. Values of Cp, H and S were obtained from statistical thermodynamic equations. The procedure was previously applied to study the thermochemical properties of indium compounds which are of interest in halide transport and OMCVD processes[19]. The study showed that energies of molecules for which experimental data were available could be calculated within a few kiloJoules and the vibrational frequencies within 10%. These calculations used values of electronic energy (including nuclear-nuclear repulsion) and vibrational harmonic frequencies obtained from quantum mechanical calculations using density functional theory[12] and the GAUSSIAN[11] program.

The thermodynamic coefficients were determined for the 47 species in this study. We used experimental values of heat of formation for the following species: $In(CH_3)_3$, $In(CH_3)_2$, $In(CH_3)$, In, C_2H_6, CH_4, CH_3, NH_3, NH_2, NH, N, H, InH_3, InH_2, InH and InN solid. All other heats of formation were derived from these experimental values and using calculated enthalpies of reaction.

2.7 Model reactor characteristics

The reactor chamber has a dimension of 30 cm along the x axis. The xz and xy cross sections have axial symmetry along the x axis. The inlet and outlet have a circular cross section with a radius of 0.71 cm. In the xz cross section, the chamber walls curve inward with a central distance of 0.8 cm, whereas in the xy cross section, the chamber walls curve outward with a maximum central distance of 2 cm; thus, the yz cross-sectional area is constant. Two substrate surfaces are located on the top and bottom chamber walls near the middle of the reactor. The horizontal dimensions of the substrates are 2 cm along the x axis and 2 cm along the y axis. Due to the wall curving of the chamber, the two parallel surfaces of the substrates are separated by 0.8 cm. The walls of the reactor are made of quartz glass (fused silica) and the substrates are made of transparent sapphire.

Because of the axial symmetry of the reactor, the model is solved numerically for a quarter of the reactor. The three-dimensional grid contains 96,960 nodes; 278,135 faces; and a total of 90,657 hexagonal cells ranging from $7.5\text{x}10^{-6}$ to

0.14 cm^3. The substrate is located immediately under the marked box shown in the middle of the central line. The white dots represent the nodes. The geometrical design of the reactor was done by the CFD Research Corporation and Sonya McCall.

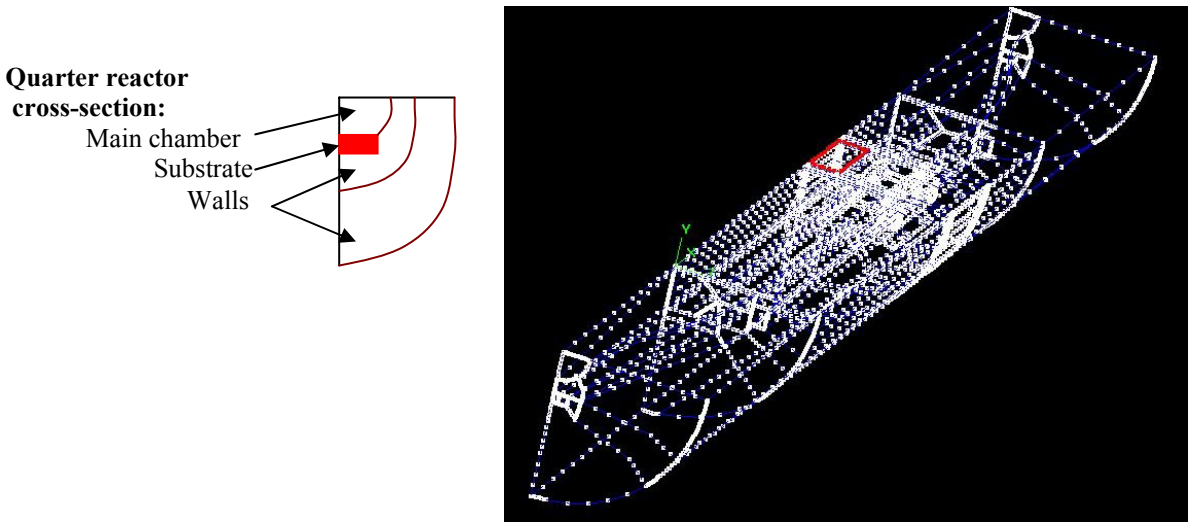

Fig. 1. Left: sketch of the cross-section of the quarter model reactor. Right: Display of the 96,960 nodes of the quarter reactor model. The flow chamber is at the top, with the center line shown going upward from the left to the right.

The background temperature selected for the simulations was 300K and for the substrate temperature was between 800 and 1400 K. The flow rates chosen were 10 standard liter per minute for N_2, and 0.25 and 50 standard cubic centimeters per minute for $In(CH_3)_3$ and NH_3, respectively. The computations were performed in three dimensions based on a quarter of the reactor. The macroscopic simulations solved the conservation equations describing fluid flow, heat and mass transfer, coupled with homogeneous and heterogeneous chemical reactions that were modeled under steady-state conditions.

3. RESULTS

In order to compare the time-evolution model with the reactor model, we computed the time needed for the gas mixture to reach and to leave the substrate. Since the reactor is represented by grids of different lengths, the time events were deduced from the velocity field.

3.1 Velocity and temperature profiles of the reactor model

Figure 2 displays the velocity profile taken at the center line of the reactor for a run that had an inlet flow velocity of 0.01 m s^{-1}, at 12.5 atm of pressure and a substrate heater set at 2.5 MW m^{-2}. The velocity increased in the region of the substrate to almost twice the inlet velocity as the temperature increased. The location of the substrate is shown by two vertical lines.

Figure 3a shows the temperature profile along the reactor chamber, taken at the interface between the gas chamber and the solid boundary. The flow reached the substrate after 5.66 s and crossed it in 0.26 s. Figure 3b shows an enlargement of the temperature profile above the substrate. Interfacial regions before and after the substrate were between 5.589 to 5.655 s and 5.916 to 5.981 s. The location of the substrate is shown with red vertical lines. The maximum temperature was 1163 K at the center of the substrate.

3.2 Dissociation of trimethylindium and ammonia

The dissociation of $In(CH_3)_3$ and NH_3 were modeled using the steady-state approach and the time-evolution model.

The dissociation of $In(CH_3)_3$ was modeled using reactions 1, 3, 4 and 76 from Table 1. This set of reactions includes the following six species: $In(CH_3)_3$, $In(CH_3)_2$, $In(CH_3)$, In, CH_3 and C_2H_6. As an example, Figure 5 displays the forward (fwd) and reverse (rvs) rate constants for the first dissociation of $In(CH_3)_3$ into $In(CH_3)_2$ and CH_3 radical, at two pressures (1 and 100 atm). Since reverse reactions are bimolecular, pressure has a bigger effect on them than on the forward reaction rates. Also, pressure has a bigger effect at higher temperatures. Because the model reactor covers temperatures between 300 to 1400 K, it was necessary to use values of rate constants suitable for that wide temperature span. The rate constants were fitted to Equation [10]. Table 2 shows the values obtained for the first dissociation of $In(CH_3)_3$ into $In(CH_3)_2$ and CH_3 at 1 and 100 atm.

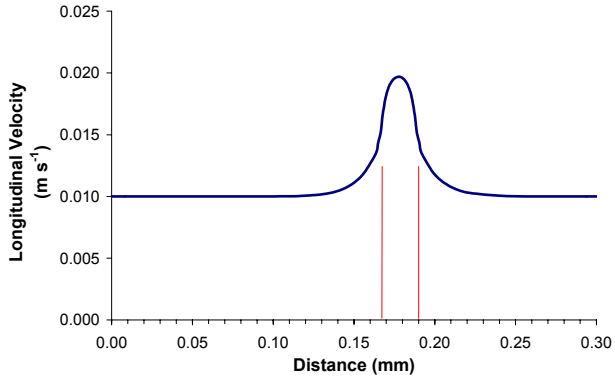

Fig. 2. Longitudinal velocity profile of the model reactor, with an inlet flow speed of 0.01 m s^{-1}. The substrate heater was set at 2.5 MW m^{-2}.

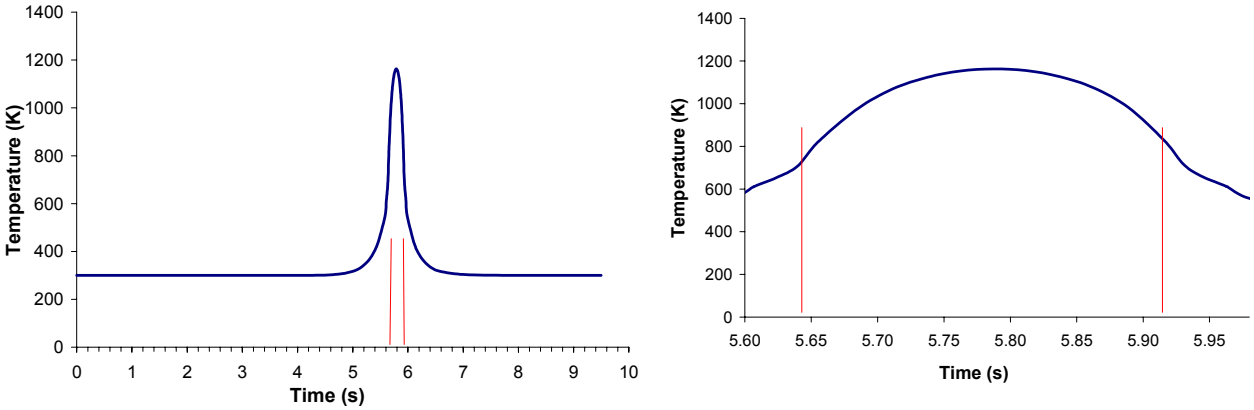

Fig.3. Temperature profile along the center line of the model reactor, with an inlet flow speed of 0.01 m s-1, a pressure of 12.5 atm, and a substrate heater set at 2.5 MW m^{-2}. a) Between the inlet and the outlet. b) Above the substrate.

The steady-state simulation for the dissociation of $In(CH_3)_3$ was performed with an inlet mass ratio of $0.9998{:}2x10^{-4}$ for nitrogen gas to $In(CH_3)_3$. The inlet flow velocity along the length of the reactor was 0.01 m s^{-1}. The substrate heater was at 2.5 MW m^{-2} and the total pressure was 12.5 atm. The maximum temperature reached at the substrate was 1163 K.

This dissociation of ammonia was represented using reactions 5-7, 78 and 79 from Table 1. This set of reactions includes six species: NH_3, NH_2, NH, N, H, N_2 and H_2. The steady-state simulation was performed with an inlet mass

ratio of $0.997{:}3x10^{-3}$ for nitrogen gas to ammonia. The inlet flow velocity along the length of the reactor was 0.01 m s^{-1}. The substrate heater was set at 2.5 MW m^{-2}. The maximum temperature reached at the substrate was 1163 K.

Figure 5 displays the average mass fractions above the substrate for the four indium species and the four nitrogen species, for the two models. The time-evolution model was set to 1163 K.

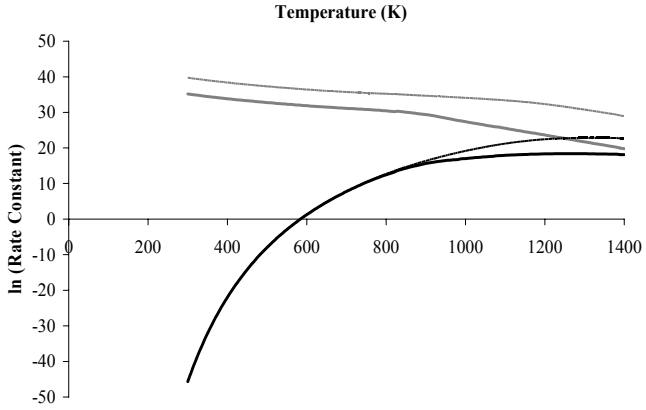

Rate constant	A*	n	Ea/R
k-fwd (1 atm)	2.223×10^{97}	-24	39985 K
k-fwd (100 atm)	1.231×10^{55}	-11	33495 K
k-rvs (1 atm)	1.496×10^{90}	-25	9986 K
k-rvs (100 atm)	5.976×10^{49}	-11	3484 K

* Units of A for k-forward (k-fwd): $s^{-1} K^{-n}$.
Units of A or k-reverse (k-rvs): $s^{-1} K^{-n} M^{-1}$.

Fig. 4. Reaction rate constants for the dissociation of $In(CH_3)_3$ to $In(CH_3)_2$ and CH_3. The thicker lines correspond to constants at 1 atm; the thinner lines to constants at 100 atm. The darker lines are the forward rate constants and the lighter lines the reverse rate constants.

Table 2. Fitting parameters for the reaction rate constants $k = A\,T^{n}\,e^{\frac{-Ea}{RT}}$ for the dissociation of $In(CH_3)_3$ into $In(CH_3)_2$ and CH_3.

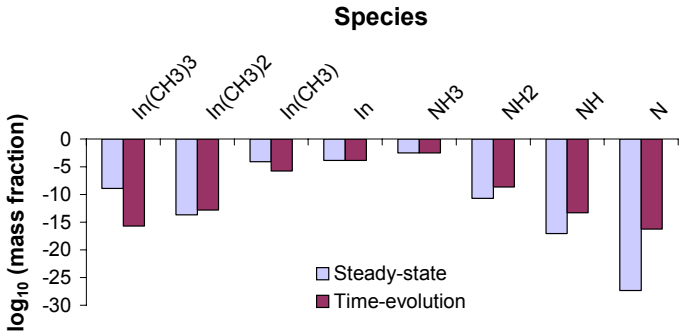

Fig. 5. Dissociation of trimethylindium and ammonia. The left bars correspond to the steady-state model and the right bars to the time-evolution model.

The larger mass fractions calculated by the two models (ammonia, at 10^{-3}, and atomic indium, in the order of 10^{-4}) were within 3% of each other. $In(CH_3)$, with a mass fraction between 10^{-5} and 10^{-6}, was 51 times larger in the steady-state model than in the time-evolution model. NH_2, with a mass fraction between 10^{-9} and 10^{-11}, was 117 times larger in the time-evolution model than in the steady state model. All other species have mass fractions below 10^{-10}. Except for $In(CH_3)_2$ and $In(CH_3)_3$, both models predict the same relative order of species. The difference between the results obtained with the two models may be attributed to: (a) effects due to flow dynamics; (b) effects due to an uneven distribution of temperatures on the substrate; and (c) the use of reaction rate constant fitted to two different equations (Equation [10] for the steady-state model and a simple Arrhenius equation for the time-evolution model).

3.3 The reduced gas model

The steady-state model is computationally intensive and substantially increases with the number of chemical reactions. Consequently, we had to select a reduced number of reactions to model the $In(CH_3)_3$-NH_3 system under different conditions. The time-evolution model was used to verify that the results from the reduced set of reactions were similar to the complete set. The scheme is shown in Figure 6. Thus, we first performed a calculation with the time-evolution model using the full set of 79 chemical reactions and 49 species (see Table 1), and selecting specific initial conditions of molar ratios, temperature and pressure. By analyzing the results, we then selected a reduced set of chemical reactions. We ran the time-evolution model on the reduced chemical set and compared the results with the full set. We modified the reduced chemical set until the results of the full set and the reduced set were similar. Finally, we used the reduced chemical set to perform the steady-state calculation and compare the results with the time-evolution model.

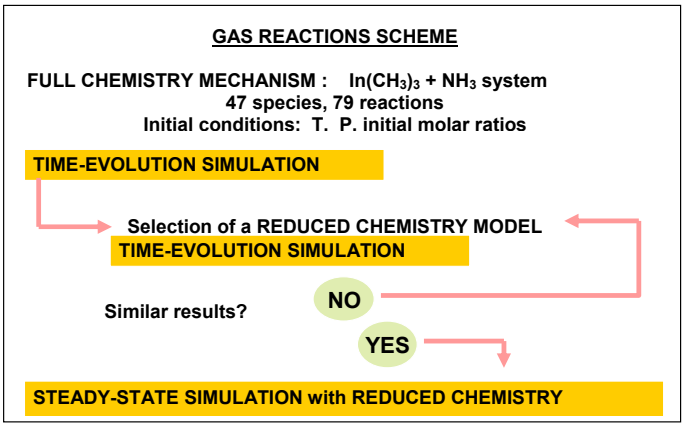

Fig. 6. Scheme for the selection of a reduced gas-phase chemical reaction model.

Figure 7 depicts an example of such calculations. The plot displays the natural logarithm of the final mass fractions of the most important species obtained using the steady-state model and the time-evolution model. The calculations were performed using a reduced system consisting of 27 species and 34 chemical reactions. The plots corresponds to the following initial conditions: N_2:NH_3:$In(CH_3)_3$ molar ratios = 0.99504:0.00493:0.00003, temperature = 1300 K, pressure = 12.5 atm. NH_2 and NH_3 are the most important group V species for both models, and In and $InCH_3$ are the most important group III species. It is interesting to see that the resulting largest molar ratios were NH_2 and In for the steady-state model, but NH_3 and $InCH_3$ for the time-evolution model, indicating that flow dynamics affects the distribution.

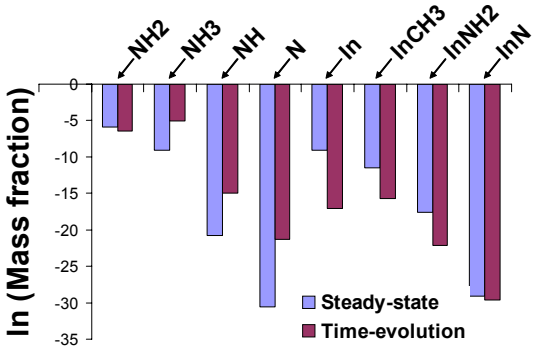

Fig 7. Final mass fractions obtained for the steady-state and the time-evolution model using a reduced set of chemical equations. Initial conditions of molar ratios: N_2:NH_3:$In(CH_3)_3$ 0.99504:0.00493:0.00003, temperature: 1300 K, pressure: 12.5 atm.

3.4 The surface reactions for the steady-state model

The formation of InN film was modeled using four paths. Since In and $In(CH_3)$ were the most abundant group III species in the gas phase (excluding species containing also nitrogen), those two species were selected to model the surface reactions for Path One and Path Two, respectively. The first path corresponded to the adsorption of atomic In and its reaction with a group V species. Since the equilibrium constant for the reaction of adsorbed In with NH_3, NH_2 and NH at 10 atm and 1100 K were calculated to be $3x10^{-6}$, $1x10^{10}$ and $2x10^{9}$, respectively, the first heterogeneous reaction selected was that of adsorbed In with NH_2. The first path consisted of the reactions 80, 84 and 85 from Table 1. Path Two corresponded to the adsorption of $InCH_3$ and its reaction with a group V species. Under similar conditions, the equilibrium constants for the reaction of adsorbed $InCH_3$ with NH_3, NH_2 and NH were calculated to be $5x10^{8}$, $1x10^{14}$ and $5x10^{10}$, respectively. Since NH_2 would be consumed by the first path, reaction with NH was selected for Path Two. The second path consisted of reactions 83, 86 and 87 from Table 1. Path Three corresponded to the direct adsorption of InN (Table 1, reaction 80). Finally, Path Four corresponded to the direct adsorption of $InNH_2$ and its dissociation into adsorbed InN and H_2 (Table 1, reactions 82 and 85). The decomposition or etching of InN film resulting from reaction 88 of Table 1 was included in each of the four paths. All paths are summarized in Table 3.

Path One	Path Two	Path Three	Path Four
In ↔ In_S	$InCH_3$ ↔ $InCH_3$_S	InN ↔ InN_S	$InNH_2$ ↔ $InNH_2$_S
In_S + NH_2 ↔ $InNH_2$_S	In CH_3_S + NH ↔ In (CH_3)NH_S	InN_S ↔ In_S + N	$InNH_2$_S ↔ InN_S + H_2
$InNH_2$_S ↔ InN_S + H_2	In(CH_3)NH_S ↔ InN_S + CH_4		InN_S ↔ In_S + N
InN_S ↔ In_S + N	InN_S ↔ In_S + N		

Table 3. Summary of selected heterogenous reactions.

3.5 Path contributions to InN growth

To compare the contribution of the four paths on the InN growth rate, we selected initial N_2:NH_3:$In(CH_3)_3$ mass ratios of 0.73:0.04:0.23. These mass ratios have been used in actual experiments[6]. The basic simulation had an inlet flow rate of 0.01 m s^{-1}, a total pressure of 10 atm, and 2.5 MW m^{-2} of substrate heating. This simulation resulted in a maximum substrate temperature of 1163 K, an average substrate temperature of 957 K, a maximum InN growth rate of 0.19 μm per hour and an average growth rate of 0.04 μm per hour. Figure 8 depicts the contributions to the growth rate resulting from the four paths. As shown in Figure 8a), 97.8% of the average growth rate came from Path One, i.e., the reaction of adsorbed In with NH_2 and its subsequent decomposition into adsorbed InN and H_2; 1.7% from Path Two (Figure 8b); a net average etching of -0.3% from Path Three (Figure 8c); and 0.8% from Path Four (Figure 8d). Note that the growth rate for Path Two becomes negative where the substrate has higher temperatures. This is due to a decrease in the available gaseous $InCH_3$ at the higher temperatures.

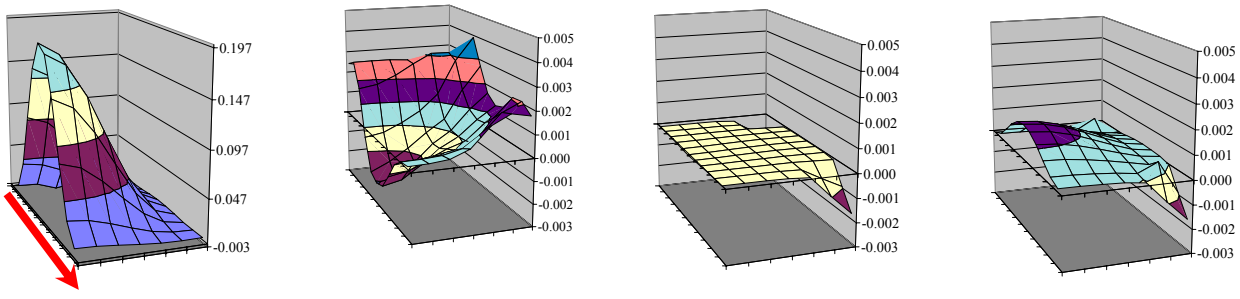

a) b) c) d)

Fig 8. InN growth rate in μm per hour. The arrow shows the direction of the flow. a) Path One: ; b) Path Two; c) Path Three; d) Path Four. Please note the change of scale between figure a) and the other figures.

3.6 Effect of substrate heating

Figure 9a) shows the temperature distribution above the substrate for this simulation. The distribution of InN growth rates shown in Figure 8a) resembles the distribution of temperatures depicted in Figure 9.

Using the same initial conditions of mass ratios, inlet flow rate and total pressure described above, simulations were also performed using different substrate heating, in order to obtain average substrate temperatures up to 1500 K. Figure 9b) shows the effect of average substrate temperature on the contribution from the various paths. One can see that Path One increased with temperature, whereas higher temperature had a detrimental effect on Path Three.

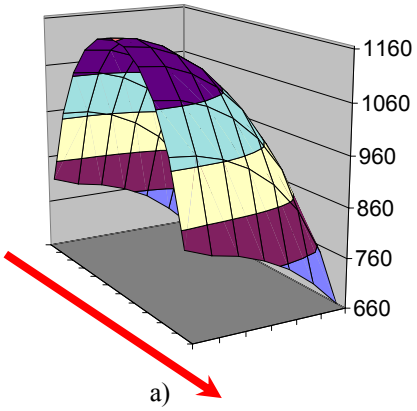

a)

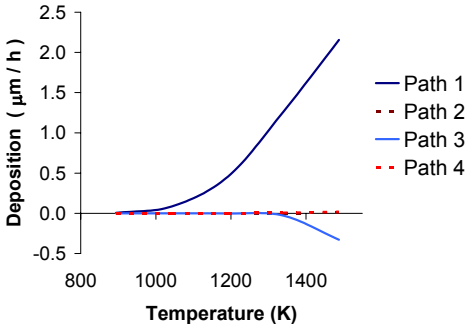

b)

Fig. 9a). Temperature distribution above the substrate in Kelvin; the arrow shows the direction of the flow. 9b). Effect of substrate temperature on the four contributions for InN growth rate.

3.7 Effect of inlet flow rate

The simulation with initial N_2:NH_3:$In(CH_3)_3$ mass ratios of 0.73:0.04:0.23, a total pressure of 10 atm, and 2.5 MW m^{-2} of substrate heating was performed using 0.01 m s^{-1} and 0.17 m s^{-1} initial flow rates. Figure 10 shows the resulting average deposition rates for these simulations. As expected, increasing the flow rate reduces the growth rate.

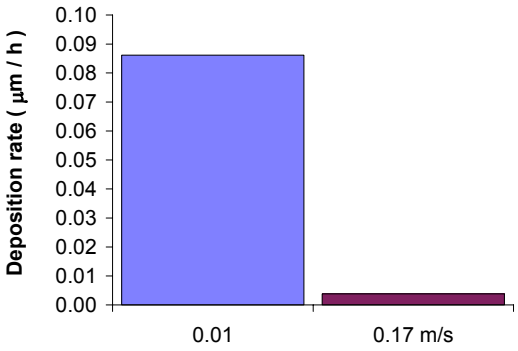

Fig. 10. Effect of inlet flow rate on the InN growth rate.

3.8 Effect of initial mass ratios

To compare the effect of doubling the amount of available group III and group V species, simulations were performed for a total pressure of 10 atm, 2.5 MW m^{-2} substrate heating, 0.01 m s^{-1}, and initial N_2:NH_3:$In(CH_3)_3$ mass ratios of 0.69:0.08:0.23 and 0.50:0.04:0.46. Figure 11 depicts the results, which should be interpreted using molar fractions.

Converting the mass ratios to molar ratios, the basic simulation had initial N_2:NH_3:$In(CH_3)_3$ molar ratios of 0.87:0.08:0.05; doubling NH_3 resulted in 0.80:0.15:0.05; and doubling $In(CH_3)_3$ in 0.77:0.10:0.12. Thus, doubling the NH_3 mass fraction increased the NH_3 mole fraction by 1.9 and had no effect on the $In(CH_3)_3$ mole fraction; whereas doubling the $In(CH_3)_3$ mass fraction, increased the NH_3 mole fraction by 1.3 and the $In(CH_3)_3$ mole fraction by 2.6.

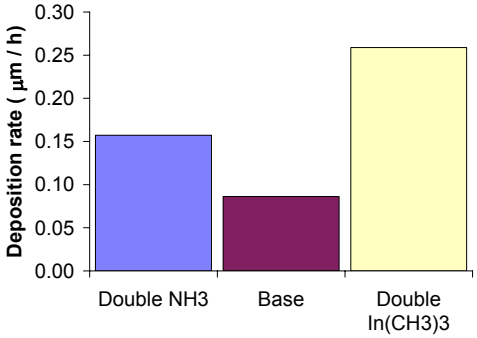

Fig. 11. Effect of doubling the initial mass ratio of NH_3 and doubling the initial mass ratio of $In(CH_3)_3$.

3.9 Effect of total pressure

To compare the effect that pressure has on the InN growth rate, be performed simulations at 10 and 20 atm. In both cases, the initial N_2:NH_3:$In(CH_3)_3$ mass ratios were 0.73:0.04:0.23, the inlet flow velocity 0.17 m s^{-1}, and the substrate heating 2.5 MW m^{-2}. Increasing the pressure had three effects: a) the average deposition rate increased by a factor of 180 times, b) the distribution of growth rates above the substrate increased toward the trailing edge of the substrate, and c) there was a change in the percent contribution from the four paths. Figure 11 shows the distribution of growth rates at 10 and 20 atm, and Figure 12 displays the percent contributions for Path One, Path Two and Path Three plus Path Four.

Fig. 11. InN growth rate in µm per hour. . The arrow shows the direction of the flow. a) At 10 atm. b) At 20 atm. Please note the change of scale between a) and b).

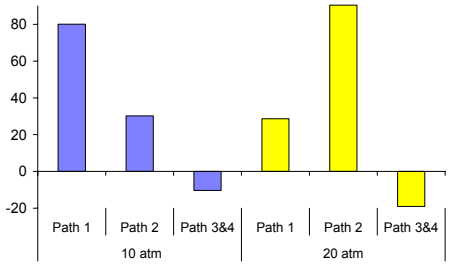

Fig. 12. Percent contribution from Path One, Path Two, Path Three plus Path Four to the InN growth rate, at 10 and 20 atm.

3.10 Validation of the steady-state model

To validate the model we choose for our steady-state simulation a set of initial conditions similar to one of the experimental values chosen by Dietz[6]. In the selected experiment, the N_2:NH_3:$In(CH_3)_3$ experimental ratios were 5.4 slm : 500 sccm : 300 sccm. We choose N_2:NH_3:$In(CH_3)_3$ mass ratios of 0.73:0.04:0.23 and an inlet flow of 0.17 m s^{-1}. The experimental reactor pressure was 10.2 bar; we selected 10 atm. The experimental reactor temperature ranged from 800 to 1150 K and the source materials were introduced through 6 s pulsing. We performed simulations at two different substrate heatings: 3.0 MW m^{-2} and 3.5 MW m^{-2}. The lower heating gave us an average substrate temperature of 1050 K and the higher heating 1290 K. The average experimental InN growth rate was 0.081 μm per hour. With the lower substrate temperature we obtained an average InN growth rate of 0.027 μm per hour and with the higher substrate temperature, 0.094 μm per hour. Figure 13 depicts the results. As can be seen, our simulations compare very well with the experimental result.

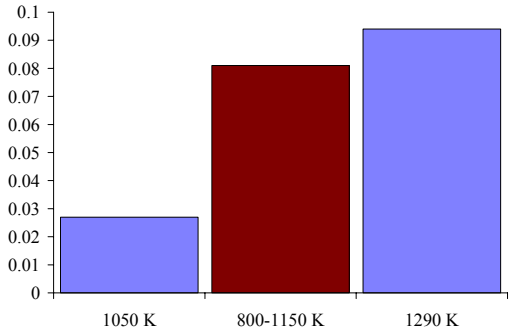

Fig. 13. Comparison between experimental and simulated average InN growth rate in μm per hour. The central bar corresponds to the experimental value, the left bar to the simulation at lower substrate heating, and the right bar to the simulation of higher substrate heating.

4. CONCLUSIONS

The results of this work can be summarized as follows:

- A high-pressure chemical vapor deposition reactor model was designed that could realistically simulate experimental results for the deposition of InN from the reaction of NH_3 and $In(CH_3)_3$.
- Reduced sets of chemical reactions could be used to represent realistically the complete set of possible chemical equations for the reaction of NH_3 with $In(CH_3)_3$.
- A simple set of heterogenous reactions, organized into four possible paths, showed that an increase on the substrate temperature could affect in opposite directions the contribution from the different paths to the overall InN growth rate.
- The average growth rate could be affected substantially by the initial molar ratios of NH_3 and $In(CH_3)_3$, as well as by the inlet flow rate.
- A change in pressure affected the InN growth rate in terms of: (a) total deposition; (b) the distribution of deposited InN over the substrate; and (c) the relative contributions from the different heterogeneous paths.
- Based on the selected simple set of heterogeneous reactions, the main paths for the formation of InN film were the deposition of atomic In and $InCH_3$, and their reaction with group V species. Direct deposition of gaseous InN and gaseous $InNH_2$ had a small effect on the InN growth rate.

ACKNOWLEDGMENTS

The authors wish to acknowledge the help received from Dr. Samuel Lowry (CFDRC) and Mr. Kenneth Walker (Media and Information Technology Center of Spelman College).

Table 1 - List of chemical reactions.

Group III source

1) $In(CH_3)_3 \leftrightarrow In(CH_3)_2 + CH_3$
2) $In_2(CH_3)_6 \leftrightarrow In(CH_3)_3 + In(CH_3)_3$
3) $In(CH_3)_2 \leftrightarrow In(CH_3) + CH_3$
4) $In(CH_3) \leftrightarrow In + CH_3$

Group V source & methyl derivatives

5) $NH_3 \leftrightarrow NH_2 + H$
6) $NH_2 \leftrightarrow NH + H$
7) $NH \leftrightarrow N + H$
8) $N(CH_3)_3 \leftrightarrow N(CH_3)_2 + CH_3$
9) $N(CH_3)_2 \leftrightarrow N(CH_3) + CH_3$
10) $N(CH_3) \leftrightarrow N + CH_3$
11) $N(CH_3)_2H \leftrightarrow N(CH_3)H + CH_3$
12) $N(CH_3)_2H \leftrightarrow N(CH_3)_2 + H$
13) $N(CH_3)H_2 \leftrightarrow NH_2 + CH_3$
14) $N(CH_3)H_2 \leftrightarrow N(CH_3)H + H$
15) $N(CH_3)H \leftrightarrow NH + CH_3$
16) $N(CH_3)H \leftrightarrow N(CH_3) + H$

Indium (methyl) hydrides

17) $In(CH_3)_2H \leftrightarrow In(CH_3)_2 + H$
18) $In(CH_3)_2H \leftrightarrow In(CH_3)H + CH_3$
19) $In(CH_3)H_2 \leftrightarrow In(CH_3)H + H$
20) $In(CH_3)H_2 \leftrightarrow InH_2 + CH_3$
21) $In(CH_3)H \leftrightarrow In(CH_3) + H$
22) $In(CH_3)H \leftrightarrow InH + CH_3$
23) $InH_3 \leftrightarrow InH_2 + H$
24) $InH_2 \leftrightarrow InH + H$
25) $InH \leftrightarrow In + H$

Group III-V adducts with trimethylindium

26) $In(CH_3)_3NH_3 \leftrightarrow In(CH_3)_3 + NH_3$
27) $In(CH_3)_3NH_3 \leftrightarrow In(CH_3)_2NH_3 + CH_3$
28) $In(CH_3)_3NH_3 \leftrightarrow In(CH_3)_3NH_2 + H$
29) $In(CH_3)_3NH_2 \leftrightarrow In(CH_3)_3 + NH_2$
30) $In(CH_3)_3NH_2 \leftrightarrow In(CH_3)_2NH_2 + CH_3$
31) $In(CH_3)_3NH_2 \leftrightarrow In(CH_3)_3NH + H$
32) $In(CH_3)_3NH \leftrightarrow In(CH_3)_3 + NH$
33) $In(CH_3)_3NH \leftrightarrow In(CH_3)_2NH + CH_3$
34) $In(CH_3)_3NH \leftrightarrow In(CH_3)_3N + H$
35) $In(CH_3)_3N \leftrightarrow In(CH_3)_3 + N$
36) $In(CH_3)_3N \leftrightarrow In(CH_3)_2N + CH_3$

Group III-V adducts with dimethylindium

37) $In(CH_3)_2NH_3 \leftrightarrow In(CH_3)_2 + NH_3$
38) $In(CH_3)_2NH_3 \leftrightarrow In(CH_3)NH_3 + CH_3$
39) $In(CH_3)_2NH_3 \leftrightarrow In(CH_3)_2NH_2 + H$
40) $In(CH_3)_2NH_2 \leftrightarrow In(CH_3)_2 + NH_2$
41) $In(CH_3)_2NH_2 \leftrightarrow In(CH_3)NH_2 + CH_3$
42) $In(CH_3)_2NH_2 \leftrightarrow In(CH_3)_2NH + H$
43) $In(CH_3)_2NH \leftrightarrow In(CH_3)_2 + NH$
44) $In(CH_3)_2NH \leftrightarrow In(CH_3)NH + CH_3$
45) $In(CH_3)_2NH \leftrightarrow In(CH_3)_2N + H$
46) $In(CH_3)_2N \leftrightarrow In(CH_3)_2 + N$
47) $In(CH_3)_2N \leftrightarrow In(CH_3)N + CH_3$

Group III-V adducts with monomethylindium

48) $In(CH_3)NH_3 \leftrightarrow In(CH_3) + NH_3$
49) $In(CH_3)NH_3 \leftrightarrow InNH_3 + CH_3$
50) $In(CH_3)NH_3 \leftrightarrow In(CH_3)NH_2 + H$
51) $In(CH_3)NH_2 \leftrightarrow In(CH_3) + NH_2$
52) $In(CH_3)NH_2 \leftrightarrow InNH_2 + CH_3$
53) $In(CH_3)NH_2 \leftrightarrow In(CH_3)NH + H$
54) $In(CH_3)NH \leftrightarrow In(CH_3) + NH$
55) $In(CH_3)NH \leftrightarrow InNH + CH_3$
56) $In(CH_3)NH \leftrightarrow In(CH_3)N + H$
57) $In(CH_3)N(CH_3)_2 \leftrightarrow In(CH_3) + N(CH_3)_2$
58) $In(CH_3)N(CH_3)_2 \leftrightarrow InN(CH_3)_2 + CH_3$
59) $In(CH_3)N(CH_3)_2 \leftrightarrow In(CH_3)N(CH_3) + (CH_3)$
60) $In(CH_3)N(CH_3) \leftrightarrow In(CH_3) + N(CH_3)$
61) $In(CH_3)N(CH_3) \leftrightarrow InN(CH_3) + CH_3$
62) $In(CH_3)N(CH_3) \leftrightarrow In(CH_3)N + (CH_3)$
63) $In(CH_3)N \leftrightarrow In(CH_3) + N$
64) $In(CH_3)N \leftrightarrow InN + CH_3$

Group III-V adducts with indium

65) $InNH_3 \leftrightarrow In + NH_3$
66) $InNH_3 \leftrightarrow InNH_2 + H$
67) $InNH_2 \leftrightarrow In + NH_2$
68) $InNH_2 \leftrightarrow InNH + H$
69) $InNH \leftrightarrow In + NH$
70) $InNH \leftrightarrow InN + H$
71) $InN(CH_3)_2 \leftrightarrow In + N(CH_3)_2$
72) $InN(CH_3)_2 \leftrightarrow InN(CH_3) + H$
73) $InN(CH_3) \leftrightarrow In + N(CH_3)$
74) $InN(CH_3) \leftrightarrow InN + H$
75) $InN \leftrightarrow In + N$

Closing reactions

76) $C_2H_6 \leftrightarrow 2\ CH_3$
77) $CH_4 \leftrightarrow CH_3 + H$
78) $N_2 \leftrightarrow 2\ N$
79) $H_2 \leftrightarrow 2\ H$

Deposition reactions

80) $InN\_S \leftrightarrow InN$
81) $In\_S \leftrightarrow In$
82) $InNH_2\_S \leftrightarrow InNH_2$
83) $InCH_3\_S \leftrightarrow InCH_3$

Surface reactions

84) $In\_S + NH_2\_S \leftrightarrow InNH_2\_S$
85) $InNH_2\_S \leftrightarrow InN\_S + H_2$
86) $In\ CH_3\_S + NH \leftrightarrow In(CH_3)NH\_S$
87) $In(CH_3)NH\_S \leftrightarrow InN\_S + CH_4$
88) $In\ N\_S \rightarrow In\_S + N$

REFERENCES

[1] T. V. Torchynska, G. P. Polupan; Semiconductor Physics, Quantum Electronics & Optoelectronics 5, 63-70 (2002)

[2] K. P. O'Donnell, I. Fernandez-Torrente, P. R. Edwards, R. W. Martin; Journal of Crystal Growth 269, 100-105 (2004).

[3] S. W. S. Chi, T.-P. Chen, C.-C. Tu, C.-S. Chang, T.-L. Tsai, M.C.C. Hsieh; Proceedings SPIE 5187, 161-170 (2004).

[4] http://www.lbl.gov/msd/PIs/Walukiewicz/02/02_8_Full_Solar_Spectrum.html. Last accessed 6/28/05.

[5] J. Torres, D. Coquillat, R. Legros, J. P. Lascaray, F. Teppe, D. Scalbert, D. Peyrade, Y. Chen, O. Briot, M. Le Vassor d'Yerville, E. Centeno, D. Cassagne, J. P. Albert; Phys. Rev. B 69, 85105-1 to 8 (2004).

[6] N. Dietz; "Indium-nitride growth by HPCVD: Real-time and ex-situ characterization"; in "GaN-based Materials: Epitaxy and Characterization", Z. C. Feng, editor; Imperial College Press (ICP), 1-31 (2005).

[7] S. J. Pearton, C. R. Abernathy, M. E. Overberg, G. T. Thaler, D. P. Norton, N. Theodoropoulou, A. F. Hebard, Y. D. Park, F. Ren, J. Kim, L. A. Boatner; J. Appl. Phys. 93, Appl. Phys. Reviews, 1-13 (2003).

[8] R. Ascázubi, I. Wilke, K. Denniston, H. Lu, W.L. Schaff; Appl. Phys. Lett. 84, 4810-4812 (2004).

[9] MATLAB, The Language of Technical Computing, Version 5.1.0.421, Copyright 1984-1997, The MathWorks, Inc.

[10] CFD-ACE; version 2003; CFD Research Corporation, Huntsville, AL 35805

[11] Gaussian03; M. J. Frisch, G. W. Trucks, H. B. Schlegel, G. E. Scuseria, M. A. Robb, J. R. Cheeseman, V. G. Zakrzewski, J. A. Montgomery, Jr., R. E. Stratmann, J. C. Burant, S. Dapprich, J. M. Millam, A. D. Daniels, K. N. Kudin, M. C. Strain, O. Farkas, J. Tomasi, V. Barone, M. Cossi, R. Cammi, B. Mennucci, C. Pomelli, C. Adamo, S. Clifford, J. Ochterski, G. A. Petersson, P. Y. Ayala, Q. Cui, K. Morokuma, P. Salvador, J. J. Dannenberg, D. K. Malick, A. D. Rabuck, K. Raghavachari, J. B. Foresman, J. Cioslowski, J. V. Ortiz, A. G. Baboul, B. B. Stefanov, G. Liu, A. Liashenko, P. Piskorz, I. Komaromi, R. Gomperts, R. L. Martin, D. J. Fox, T. Keith, M. A. Al-Laham, C. Y. Peng, A. Nanayakkara, M. Challacombe, P. M. W. Gill, B. Johnson, W. Chen, M. W. Wong, J. L. Andres, C. Gonzalez, M. Head-Gordon, E. S. Replogle, and J. A. Pople, Gaussian, Inc., PA, (2003).

[12] R. G. Parr, W. Yang; "Density-functional theory of atoms and molecules"; Oxford Univ. Press, Oxford, 1989; A. D. Becke; J. Chem. Phys. 104, 1040 (1996)

[13] R. A. Marcus; J.Chem. Phys, 20, 359 (1952)

[14] J. J. Troe; J. Chem. Phys., 66, 4745-57 (1977); J. Chem. Phys., 66, 4758-75 (1977)..

[15] B. H. Cardelino, C. E. Moore, C. A. Cardelino, S. D. McCall, D. O. Frazier, K. J. Bachmann; "Semiclassical calculation of reaction rate constants for homolytical dissociation reactions of interest in OMCVD"; J. Physical Chemistry A 107, 3708-3718 (2003).

[16] S. Dapprich, I. Komaromi, K. S. Byun, K. Morokuma, M. J. Frisch; "A New ONIOM Implementation in Gaussian98. Part I: The Calculation of Energies, Gradients, Vibrational Frequencies and Electric Field Derivatives"; J. Mol. Struct. (Theochem) 462, 1-21 (1999).

[17] D. Sengupta, S. Mazumder, W. Kuykendall, S. A. Lowry; J. Crystal Growth 279, 369-382 (2005).

[18] M. W. Chase; "JANAF Thermochemical Tables"; American Chemical Society (Washington, DC) and American Institute of Physics (New York, NY) for the National Bureau of Standards; issued as Supplement #1 to Volume 14 of the Journal of Physical and Chemical Reference Data; 3rd edition (1986).

[19] B. H. Cardelino, C. E. Moore, C. A. Cardelino, D. O. Frazier, K. J. Bachmann; J. Phys. Chem. A, 105, 849-868 (2001)